

# A Study on the Microstructures and Toughness of Fe-B Cast Alloy Containing Rare Earth

Dawei Yi, Zhiyun Zhang, Hanguang Fu, Chengyan Yang, Shengqiang Ma, and Yefei Li

(Submitted November 10, 2013; in revised form September 15, 2014; published online December 2, 2014)

This study investigates the effect of cerium on the microstructures, mechanical properties of medium carbon Fe-B cast alloy. The as-cast microstructure of Fe-B cast alloy consists of the eutectic boride, pearlite, and ferrite. Compared with the coarse eutectic borides in the unmodified alloy, the eutectic boride structures in the modified alloy are greatly refined. Cerium promotes the formation of  $Ce_2O_3$  phase.  $Ce_2O_3$  can act as effective heterogeneous nuclei of primary austenite, and refine austenite and boride. After heat treatment, the impact toughness of the modified alloy is higher than that of the unmodified alloy because there are more broken borides in the modified alloy. Meanwhile, the fracture mechanism of medium carbon Fe-B alloy is depicted and analyzed by using fractography.

**Keywords** boride, cerium, impact toughness, microstructure

## 1. Introduction

High chromium white cast irons have superior wear resistance and are widely used in mineral processing, cement production, thermal electric power plants, and others (Ref 1-3). Their exceptional wear resistance is the result of their high carbon and chromium concentrations, which form  $(Cr,Fe)_7C_3$  carbides along with austenite during solidification. However, high chromium white cast irons suffer from shortcomings such as high concentration of alloying elements, exorbitant production cost, and propensity for deformation and fracture after heat treatment (Ref 4). So, the development of new type wear-resistant material is very important.

The studies of boronizing reveal that a  $Fe_2B$  layer produces superior wear resistance and mechanical properties (Ref 5, 6). This makes it possible to apply  $Fe_2B$  as the wear-resistant phase. According to Fe-B phase diagram (Ref 7), boron has a very low solubility in  $\alpha$ -iron (0.0081 wt.%) and  $\gamma$ -iron (0.02 wt.%). So, this makes the formation of boride possible when boron is added in iron melt. Because of high boron concentration, the solidification process of Fe-B alloy is summarized as follows: First, the primary  $\gamma$  phase separates out from the melt. Since the partition coefficients of elements

such as chromium, manganese, and boron are lower than one in  $\gamma$  phase (Ref 8), these elements will be discharged into melt accompanied by the growth of the  $\gamma$  phase. When the boron concentration in the melt nears 3.8 wt.%, the eutectic reaction occurs in the remnant melt (Ref 7). Therefore, the addition of boron promotes the formation of eutectic boride.

Moreover, the boride has high hardness, and therefore, can be taken as the strengthening phase. This information would be helpful to develop a new type of wear-resistant material. The conspicuous advantage of Fe-B alloy is that the matrix and boride could be controlled, respectively, by carbon and boron contents. In this case, the strengthening and toughening matrix and adequate volume percentage of boride could be obtained at the same time, which would make it possible to design the microstructure that we need (Ref 9).

Fe-B alloy has such characteristics as excellent wear resistance, low alloying content, simple casting process, and low production costs (Ref 10, 11). The application of the Fe-B alloy is helpful for the decrease of material consumption due to its high abrasion resistance and toughness (Ref 12). However, there exist many coarse borides, which are not favorable to the improvement of the strength and toughness of Fe-B alloy. Fu et al. (Ref 13) studied the effects of rare earth and titanium additions on the microstructures and properties of low carbon Fe-B alloys, and pointed out that proper modification using rare earth combined with titanium can refine the grain size of primary austenite and increase the impact toughness of the Fe-B alloy. However, the refinement mechanism of rare earth in the Fe-B alloy should be further studied.

The purpose of present research is to study the microstructures and impact toughness of a Fe-B cast alloy modified by cerium. As a result, the as-cast eutectic boride microstructures are greatly refined, and the impact toughness increases when cerium is added.

## 2. Experimental Procedures

### 2.1 Melting, Casting, and Heat Treatment of Fe-B Cast Alloy

The alloys used for this investigation were melted in a 10 kg capacity medium-frequency induction furnace using a quartzite

**Dawei Yi** and **Zhiyun Zhang**, School of Materials Science and Engineering, Xi'an University of Science and Technology, 58 Yanta Road, Xi'an 710054 Shaanxi Province, People's Republic of China; **Hanguang Fu**, Research Institute of Advance Materials Processing Technology, School of Materials Science and Engineering, Beijing University of Technology, Beijing 100124, People's Republic of China; **Chengyan Yang**, Foundry, Zibo Diesel Engine Company, Zibo 255077 Shandong Province, People's Republic of China; and **Shengqiang Ma** and **Yefei Li**, State Key Laboratory for Mechanical Behavior of Materials, School of Materials Science and Engineering, Xi'an Jiaotong University, Xi'an 710049 Shaanxi Province, People's Republic of China. Contact e-mail: yidawei19820608@163.com.

lining. Initial charge materials contained clean pig iron and steel scrap. When these initial charge materials were melted, Fe-61.5 wt.% Cr alloy, Fe-65.8 wt.% Mn alloy, Fe-75.3 wt.% Si alloy, and copper were added to molten alloy. When the temperature of molten alloy was up to 1610 °C, Fe-16.1 wt.% B alloy, and Fe-26.5 wt.% Ti alloy were added to the melt. After deoxidation by pure aluminum, the molten alloy was modified using Fe-63.4 wt.% Cr-12.6 wt.% N alloy and Fe-39.4 wt.% Ce-24.2 wt.% Si alloy when it was poured into the ladle (before pouring, the modifier had been placed in the ladle) and then was poured at 1470 °C into a sand mold. The specimens were austenized at 1050 °C for 4 h using box-type resistance furnace (with argon protection), followed by quenching in water. Subsequently, the specimens were tempered at 180 °C for 4 h. The chemical compositions of the alloy, determined by optical emission spectroscopy, are shown in Table 1.

## 2.2 Microstructure Examination

The geometry of sand mold and specimens is shown in Fig. 1. The red rectangle (in Fig. 1b) of approximate dimension

20 × 20 × 10 mm was sliced. The metallographic analysis was carried out on the “polished surface” (the polished surface is 40 mm to the bottom of rectangle sample, see Fig. 1b). Before this analysis, the polished surface was etched by 5% nital. Furthermore, the microindentation hardness was also measured at this polished surface.

The metallographic analysis techniques used for material structure included optical microscope (OM), scanning electron microscope (SEM), x-ray diffraction (XRD), and transmission electron microscope (TEM). The OM employed was Neophot 21. The SEM employed was a JEOL JSM-6360LV and a Noran System Six microscope equipped with an energy dispersive x-ray spectrometry (EDS). XRD was performed on a D/MAX-2400 diffractometer with Cu K $\alpha$  radiation at 40 kV and 100 mA as an x-ray source. The specimen was scanned in the  $2\theta$  range of 20°-85° in a step scan mode (0.02° per step). The TEM used was a JEM-200CX, and the TEM specimens (the diameter is 3 mm and the thickness is 50  $\mu$ m) were prepared by electrolytic polishing at 30 V, using a solution of 5% perchloric acid and 95% methanol at 0 °C.

**Table 1** Chemical compositions of Fe-B alloys (wt.%)

Specimens	C	B	Cr	Cu	Mn	Si	Ce	Fe
C <sub>0</sub>	0.31	1.05	1.10	0.46	0.81	0.51	0	Bal.
C <sub>1</sub>	0.27	1.08	1.06	0.42	0.79	0.58	0.13	
C <sub>2</sub>	0.31	1.08	1.11	0.52	0.84	0.55	0.36	
C <sub>3</sub>	0.28	1.07	1.07	0.47	0.86	0.61	0.54	

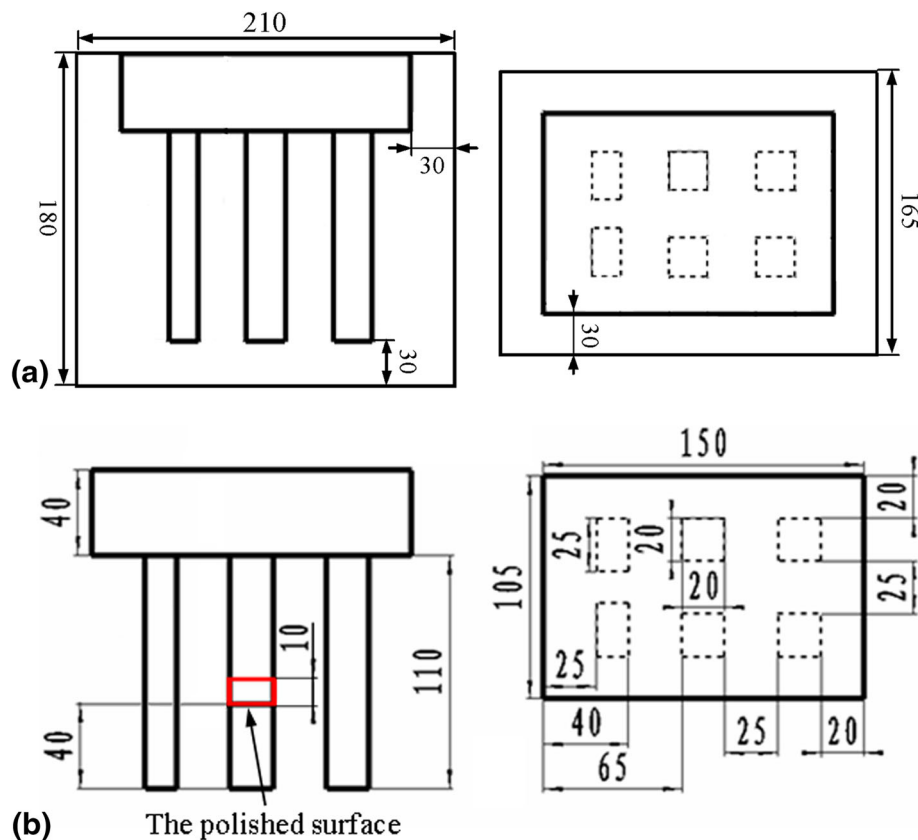


**Fig. 1** Schematic (unit in mm) of sand mold (a) and specimens (b) (Color figure online)

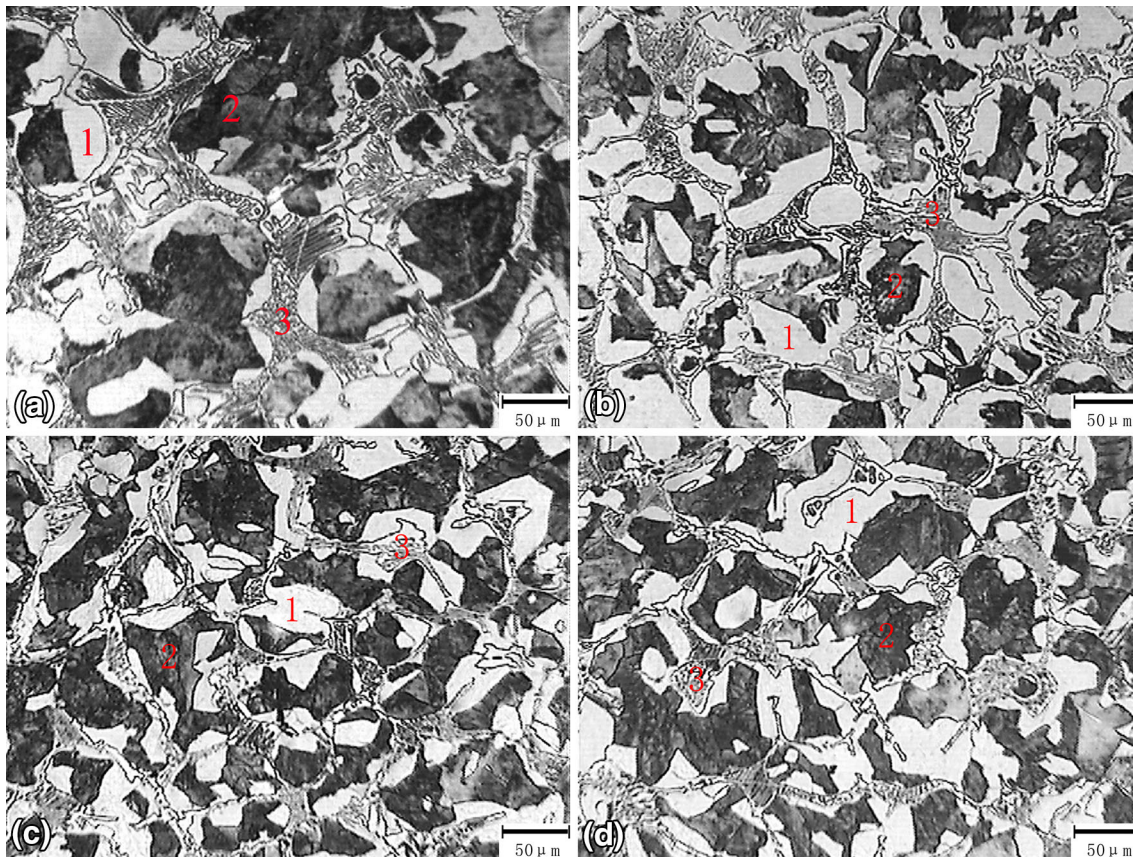


**Fig. 2** Solidification microstructures of as-cast Fe-B alloys: (a)-(d) showing 200 times magnification structures of C<sub>0</sub>, C<sub>1</sub>, C<sub>2</sub>, and C<sub>3</sub> alloys, respectively; 1—ferrite; 2—pearlite; 3—Fe<sub>2</sub>B

Leica digital image analyzer was used for analyzing the number of grains per square millimeter ( $n_a$ ). The number of grains per square millimeter ( $n_a$ ) in one image, measured by area method (a circle of 50 mm diameter), is gained from (Ref 14):

$$N = N_{\text{Inside}} + \frac{1}{2}N_{\text{Intercepted}} - 1 \quad (\text{Eq 1})$$

$$n_a = \frac{M^2 \cdot N}{A_0}, \quad (\text{Eq 2})$$

where  $N_{\text{Inside}}$  is the number of grains completely inside the test circle,  $N_{\text{Intercepted}}$  is the number of grains that intercept the test circle,  $N$  is the number of grains related to the test circle,  $M$  is the magnification of images, and  $A_0$  is the area of the test circle.

At a magnification of 50 times, 20 images of the specimen were randomly selected to calculate  $n_a$ , and the test result was the average value of 20 measurements.

### 2.3 Hardness and Impact Toughness Tests

Microindentation hardness was measured on a HXD-1000TMC tester according to American Society for Testing and Materials (ASTM) standard E384-08 (Ref 15), and 0.98 and 0.49 N were the applied loads for borides and matrix, respectively. The full test force was kept for 10 s. Twenty indentations were made on each specimen to check the reproducibility of hardness data. The HRS-150 Rockwell

hardness tester was used to measure the room temperature hardness, and the applied load was 1470 N. The test result was the average value of ten measurements.

The unnotched impact tests were performed at room temperature by JB-300B impact testing device. The anvil span length was 70 mm, and the impact energy was 300 J. The unnotched impact specimen size (rectangle sample) was 20 × 20 × 110 mm. The impact toughness value was the average of six specimens.

## 3. Results and Discussion

### 3.1 Solidification Microstructures of Fe-B Alloy

The microstructures of Fe-B alloys with different cerium concentrations are exhibited in Fig. 2. Figure 3 shows the XRD spectrum of C<sub>0</sub>, C<sub>1</sub>, C<sub>2</sub>, and C<sub>3</sub> alloys. Figure 4 shows the microindentation hardness of metallic matrix in Fe-B alloys. Figure 2 indicates that the microstructures of Fe-B alloys are composed of the eutectic boride and metallic matrix (Ref 16). The eutectic boride is proved to be Fe<sub>2</sub>B (area “3” in Fig. 2) by XRD (Fig. 3a-d); while the metallic matrix is composed of the ferrite (area “1” in Fig. 2) and pearlite (area “2” in Fig. 2) because the hardness values are in accordance with their natural hardnesses (Ref 16).

The backscattered electron (BSE) micrographs of C<sub>1</sub> and C<sub>3</sub> alloys are shown in Fig. 5. Figure 5 displays that the number of

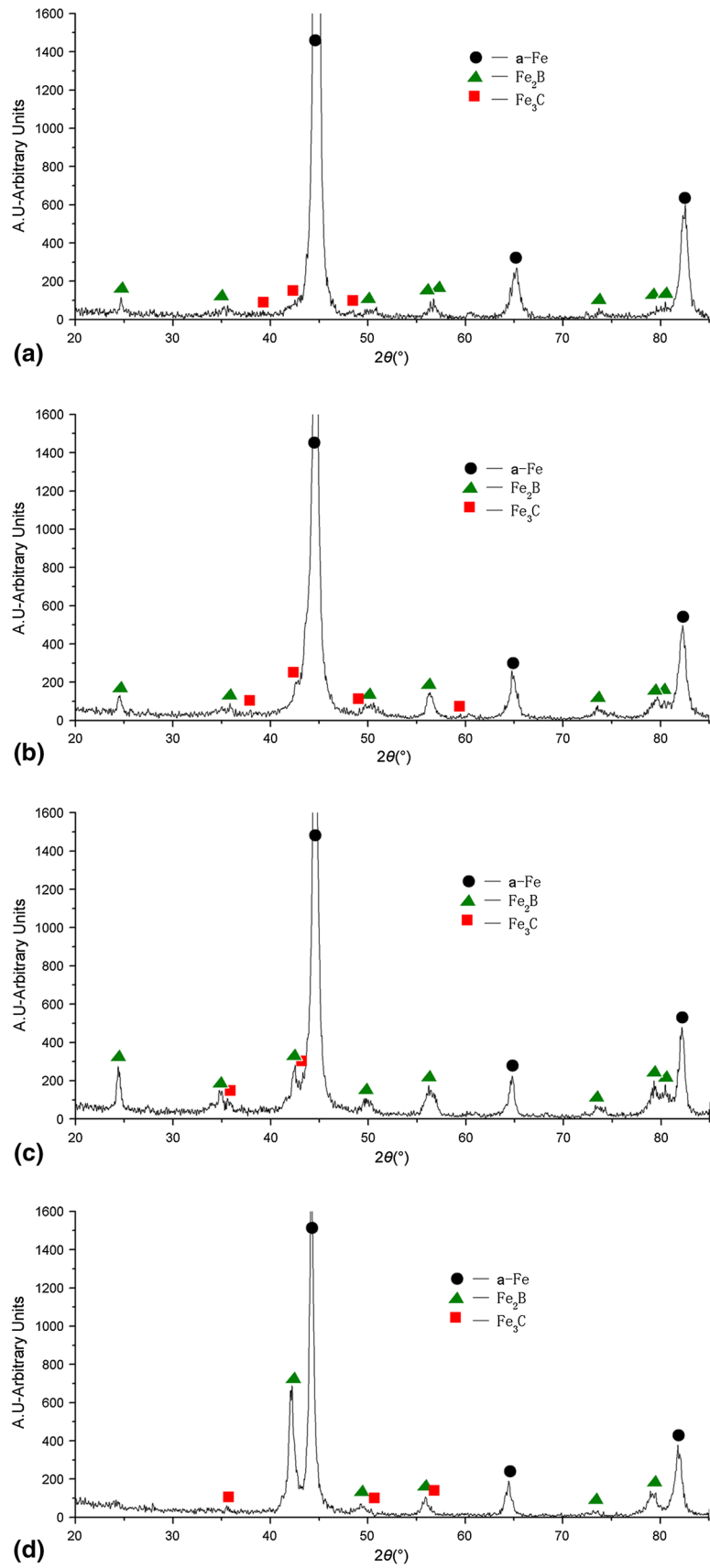


**Fig. 3** X-ray diffraction spectrum of as-cast alloys



cerium compounds (white particles) increase with the increase of cerium concentration (Fig. 5a and b). The corresponding EDS spectrum at point A in Fig. 5(c) reveals that Ce and O elements are present. Figure 6 shows the bright field TEM micrograph and corresponding selected area diffraction pattern of cerium compound in C<sub>3</sub> alloy. The electron diffraction pattern proves that the dark region is close-packed hexagonal

structure. These results indicate the existence of Ce<sub>2</sub>O<sub>3</sub> particles in Fe-B alloy modified by cerium (Ref 17).

The number of grains per square millimeter ( $n_a$ ) of Fe-B alloys is shown in Fig. 7. It can be seen from Fig. 7 that the alloys containing cerium have higher  $n_a$  than that in the unmodified alloy (C<sub>0</sub> alloy), and  $n_a$  of C<sub>2</sub> alloy is slightly lower than that of C<sub>3</sub> alloy. The refinement of the eutectic boride

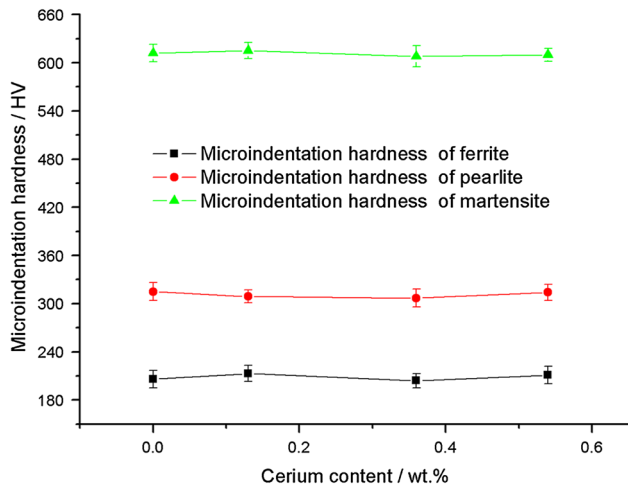


Fig. 4 Microindentation hardness of metallic matrix in Fe-B alloys

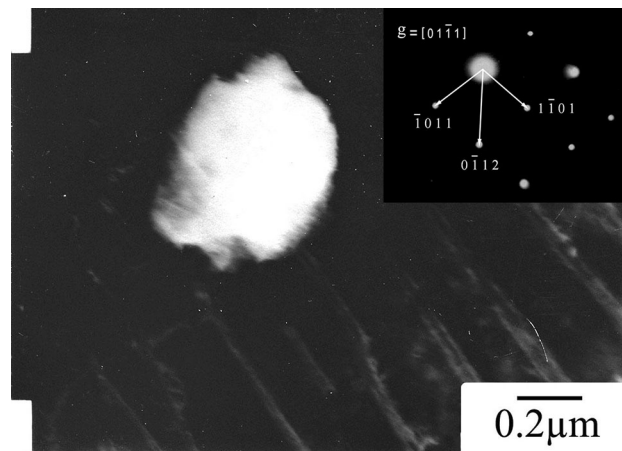


Fig. 6 Bright field transmission electron microscope micrograph and corresponding selected area diffraction pattern of cerium oxide in as-cast C<sub>3</sub> alloy

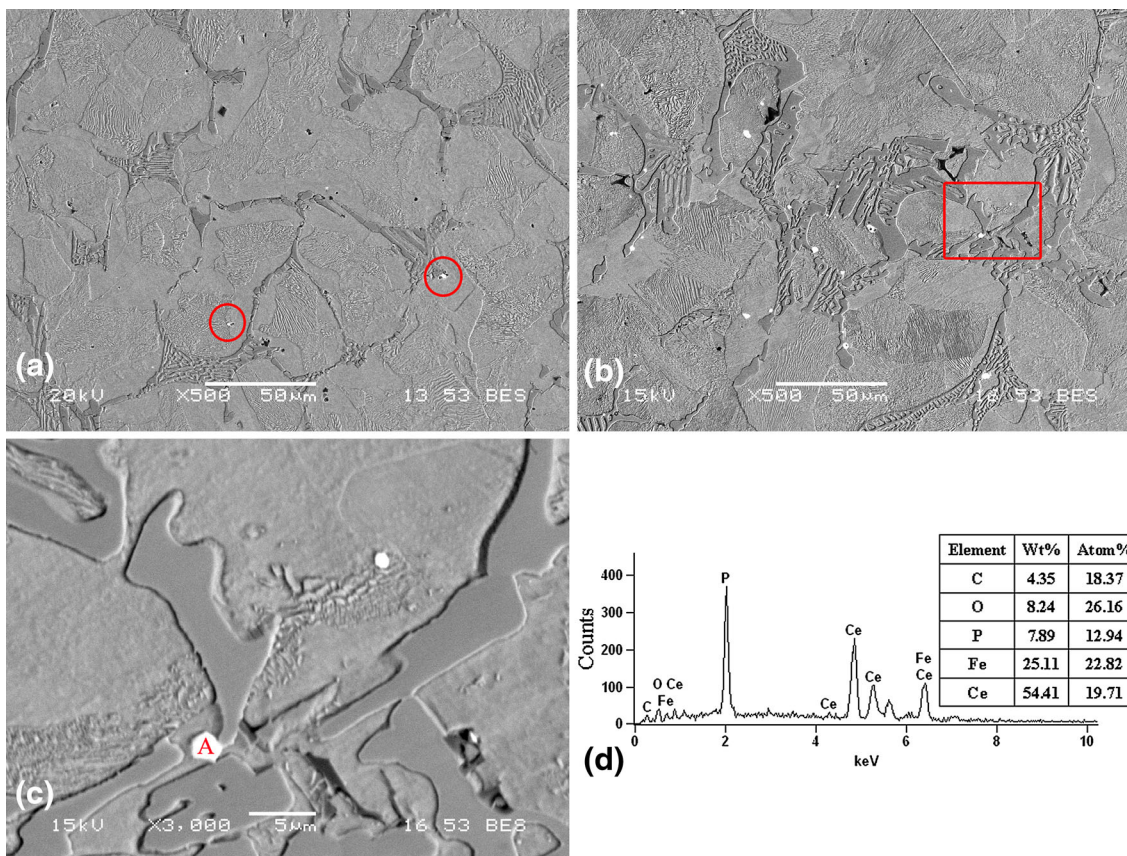
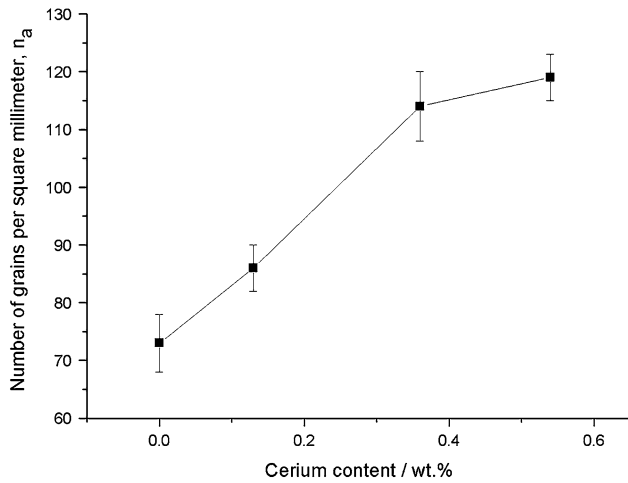


Fig. 5 SEM and distribution of cerium in Fe-B alloys: (a) showing BSE micrograph of C<sub>1</sub> alloy; (b) and (c) showing BSE micrographs of C<sub>3</sub> alloy; (d) showing EDS spectra of point A (c)

would be promoted by the fine matrix grains. So, the microstructures of  $C_0$  alloy (Fig. 2a) show the coarse eutectic borides along grain boundaries. Compared with  $C_0$  alloy, more refined eutectic borides in modified alloys are obtained (Fig. 2b-d). Some researchers studied the microstructure of

Fe-B cast alloy modified by neodymium (Ref 18), their result showed that the neodymium could refine the as-cast microstructure. These results reveal that the rare earth (neodymium and cerium) in Fe-B alloy should be effective modifiers for microstructure refinement.



**Fig. 7** The number of grains per square millimeter of Fe-B alloys

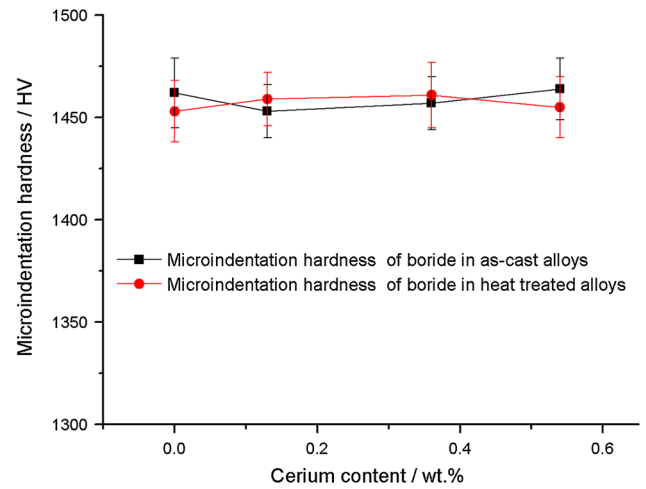


**Fig. 9** Microindentation hardness of boride in Fe-B alloys

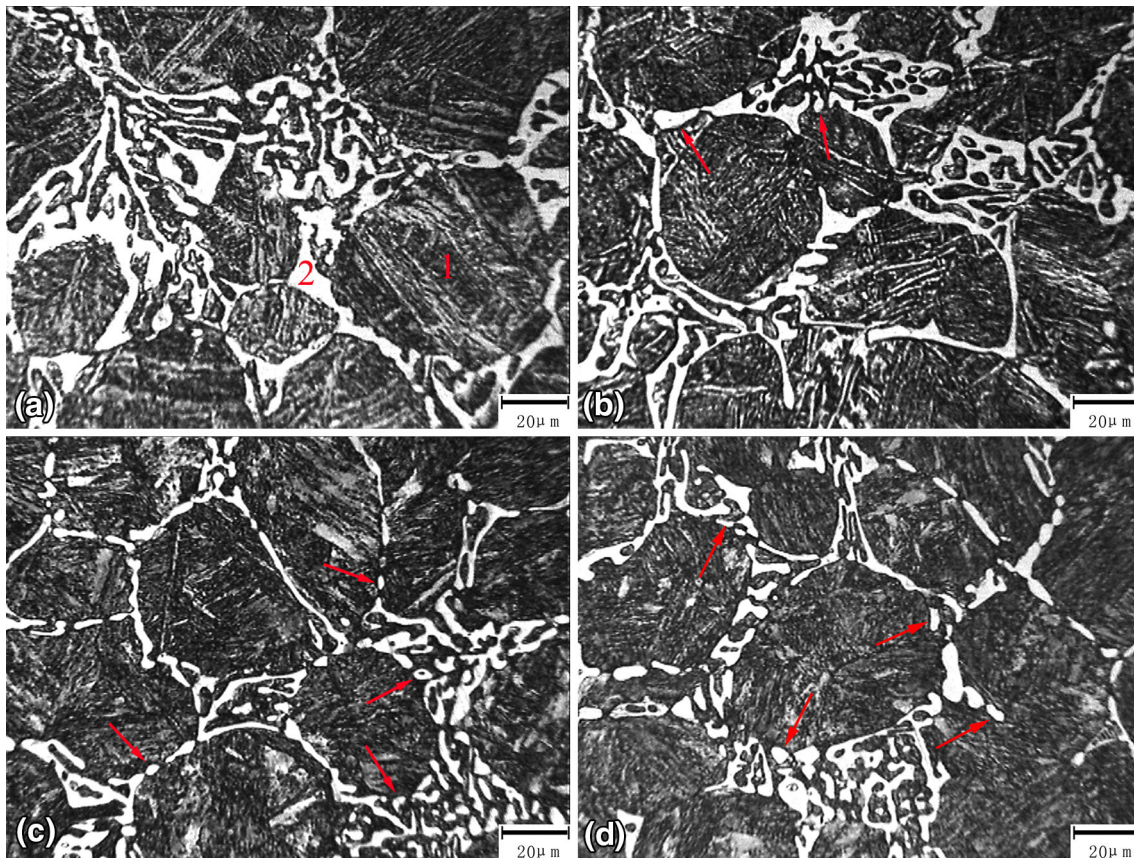


**Fig. 8** Heat-treated microstructures of Fe-B alloys: (a)-(d) showing 500 times magnification microstructures of  $C_0$ ,  $C_1$ ,  $C_2$ , and  $C_3$  alloy, respectively; 1—martensite; 2— $Fe_2B$  (Color figure online)



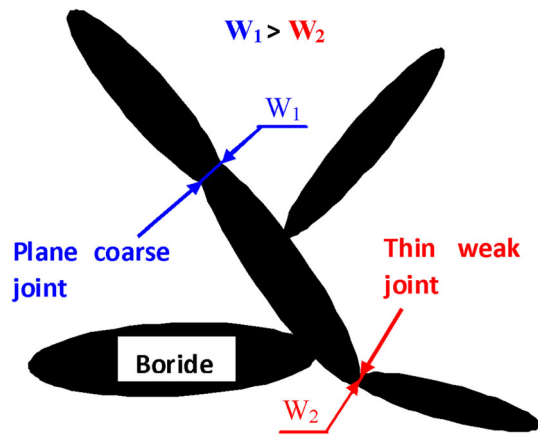


Fig. 10 Schematic diagram of boride network in Fe-B alloy

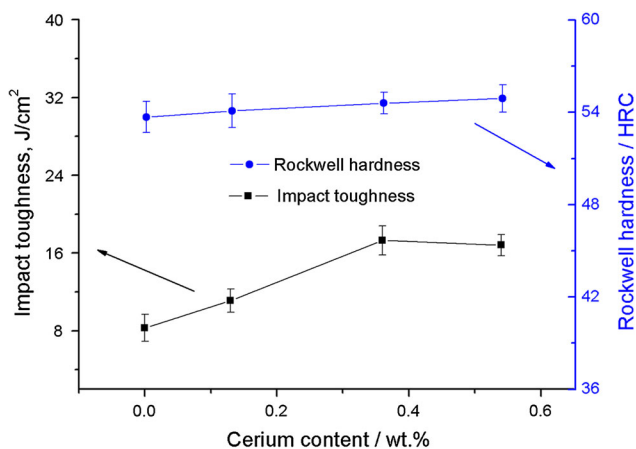


Fig. 11 Rockwell hardness and impact toughness of Fe-B alloys

### 3.2 Heat-Treated Microstructures of Fe-B Alloy

The microstructures of heat-treated  $C_0$ ,  $C_1$ ,  $C_2$ , and  $C_3$  alloys are shown in Fig. 8. Figure 9 displays the microindentation hardness of the boride. The microindentation hardness analysis (Fig. 4 and 9) reveals that the eutectic boride and metallic matrix would be  $Fe_2B$  (white phase in Fig. 8) and martensite (black phase in Fig. 8) (Ref 19). Moreover, compared with as-cast metallic matrix (ferrite and pearlite), the heat-treated metallic matrix (martensite) has higher microindentation hardness.

It can be seen from Fig. 8(a) that a few of eutectic boride networks are broken in  $C_0$  alloy. Compared with  $C_0$  and  $C_1$  alloy, there are more broken borides in  $C_2$  and  $C_3$  alloy, and their morphology is short rod-shaped and round (the red arrows in Fig. 8c and d). Generally, the number of broken borides increases with the increase of  $n_a$  (the number of grains per square millimeter). These results prove that cerium is helpful for breakdown of the eutectic boride during heat treatment.

During heat treatment, the boride in Fe-B alloy changes from strip morphology to spheroidized morphology. The thermodynamic driving force comes from the decrease of free energy between eutectic boride and matrix interface. The kinetic driving force is the diffusion of the boron atom on the boride/matrix interface. At high temperature, the diffusion of boron atoms along the boride/matrix interface results in part of the eutectic boride dissolving in the matrix and then precipi-

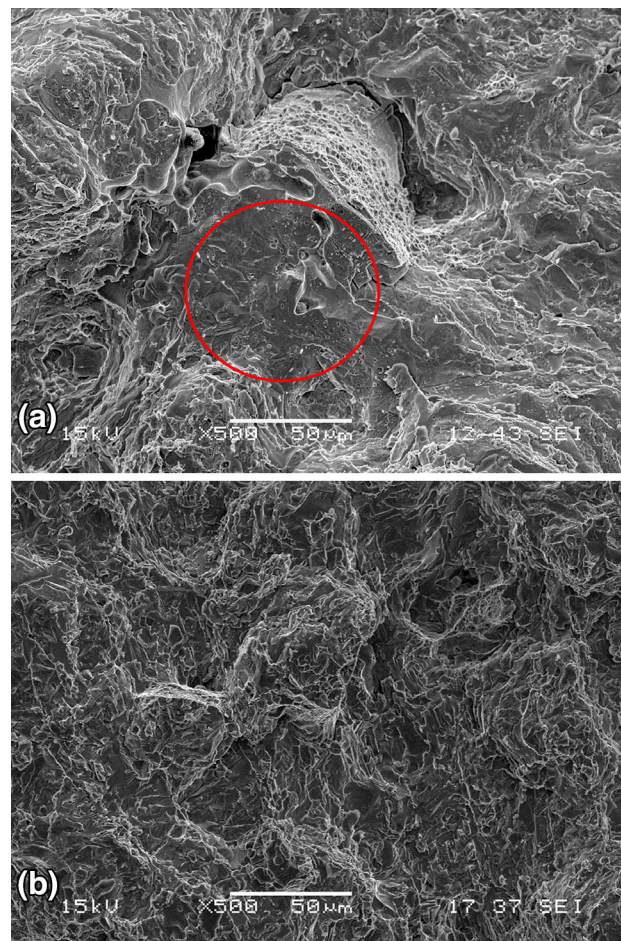


Fig. 12 Fractographies of impact test specimens: (a)  $C_0$  specimen; (b)  $C_2$  specimen (Color figure online)

tating on boride itself (Ref 20). So, the spheroidized boride forms during high temperature heat treatment. The schematic diagram of the boride network in Fe-B alloy is shown in Fig. 10. It can be seen that the plane coarse joint and thin weak joint exist in the boride network. The diffusion of boron at the thin weak joint (low  $W_2$ ) is easier and faster than at the plane coarse joint (high  $W_1$ ) (Ref 20, 21), therefore, the breaking of the fine boride network in modified alloy is easier than coarse boride network in unmodified alloy ( $C_0$ ).

### 3.3 The Hardness and Impact Toughness of Fe-B Alloy

The Rockwell hardness and impact toughness of Fe-B alloys with different cerium concentrations are shown in Fig. 11. From Fig. 11, it can be seen that the Rockwell hardness increases slightly with rising cerium concentration. The increasing hardness could be caused by the microstructure refinement. Moreover, the impact toughness value increases with the increase in cerium concentration. Figure 8 and 11 reveal that the more the number of broken borides, the higher is the impact toughness value.

The fractographies of  $C_0$  and  $C_2$  impact specimens are shown in Fig. 12. The theory of the fracture mechanics points out that, the brittle fracture includes initiation and propagation of the crack (Ref 22), which is determined by the matrix and the amount, size, and morphology of the borides in the Fe-B alloys. Because all the metallic matrices of heat-treated Fe-B alloys are

martensitic, the initiation and propagation of the crack will be determined by the amount, size, and morphology of the borides.

In  $C_0$  alloy, the boride networks are coarse and concentrated (Fig. 8a), the cracks are easy to form and propagate along the coarse borides, and some big cleavage planes are left on the fracture (see the red circle in Fig. 12a). In this case, the impact toughness will be low. However, in  $C_2$  alloys, the breaking of boride networks is apparent, and the broken borides are fine and dispersed (Fig. 8c). The appearance of local broken boride networks can reduce crack propagation along the boride networks effectively. In this situation, the big cleavage plane will not appear (Fig. 12b), and high impact toughness value is realized (Ref 19).

### 3.4 The Refinement Mechanism of Cerium on the Boride

Rare earth elements can act to deoxidise the steel, and decrease the content of oxygen by combining with them to form rare earth compounds (Ref 17). In the present study, from Fig. 5 and 6 (SEM, EDS, and TEM), the existence of  $Ce_2O_3$  phase in Fe-B alloys (with cerium) has been proved. According to the formula in Ref 23, the  $\Delta G$  of  $Ce_2O_3$  at the temperature of 1500 °C is  $-688,606$  J/mol, which indicates that  $Ce_2O_3$  can be formed at the temperature of 1500 °C and can exist stably in the melt when cerium is added. This calculation reveals that  $Ce_2O_3$  particles can precipitate before the formation of primary austenite (Ref 13, 23).

The value of the two-dimensional lattice misfit is used to estimate whether  $Ce_2O_3$  can act as the heterogeneous nuclei of primary austenite. A mathematical model of the two-dimensional lattice misfit (Ref 24) is

$$\delta_{(hkl)_n}^{(hkl)_s} = \sum_{i=1}^3 \frac{|d_{[uvw]_s}^i \cos \theta - d_{[uvw]_n}^i|}{d_{[uvw]_n}^i} \times 100, \quad (\text{Eq 3})$$

where the  $(hkl)_s$  is the low index crystal face of the nucleus, the  $[uvw]_s$  is the low index crystal orientation in the  $(hkl)_s$ , the  $(hkl)_n$  is the low index crystal face of the new crystal phase, the  $[uvw]_n$  is the low index crystal orientation in the  $(hkl)_n$ ,  $d_{[uvw]_s}^i$  and  $d_{[uvw]_n}^i$  are the atomic spacing along the  $[uvw]_s$  and the  $[uvw]_n$ , respectively,  $\theta$  is the angle included between the  $[uvw]_s$  and the  $[uvw]_n$  ( $\theta < 90^\circ$ ). Bramfitt proposed a theory (Ref 25) that during heterogeneous nucleation, the nuclei with  $\delta < 6\%$  are the most effective, while those with  $\delta$  between 6 and 12% are medium effective and those with  $\delta > 12\%$  are ineffective.

The structure of  $Ce_2O_3$  is close-packed hexagonal. Its lattice parameters are as follows:  $a = 0.3927$  nm and  $c = 0.6062$  nm. The primary austenite ( $\gamma$ ) has a face-centered cubic structure. The lattice parameter of primary austenite is 0.3726 nm. The calculation reveals that the lattice misfit between  $(0001)_{Ce_2O_3}$  and  $(111)_\gamma$  is 5.4% (Ref 26). Consequently,  $Ce_2O_3$  can act as effective heterogeneous nuclei of primary austenite and facilitate the refinement of austenite. The fine austenite will promote the refinement of borides during solidification, and the fine borides are in favor of broken boride network appearance during heat treatment (Ref 13).

## 4. Conclusions

The eutectic borides in medium carbon Fe-B cast alloy were refined by cerium addition. This work demonstrates the following conclusions:

- (1) The as-cast microstructures of Fe-B alloys are composed of ferrite, pearlite, and eutectic boride. The number of grains per square millimeter in Fe-B alloys with cerium addition is higher than that in unmodified alloy. Moreover, compared to the coarse eutectic borides in unmodified alloy, the eutectic boride in Fe-B alloys modified by cerium are greatly refined.
- (2) After heat treatment, compared with unmodified alloy, there are more short rod-shaped and round borides in the modified alloy. Moreover, the impact toughness of Fe-B alloys containing cerium is higher than that of the unmodified alloy. The change of boride morphology from continuous network to disconnected network should be the main reason.

## Acknowledgments

This work was supported by Scientific Research Program Funded by Shaanxi Provincial Education Department (2013JK0919), the Research Foundation of Xi'an University of Science and Technology (2013QDJ026, 2012QDJ034, and 201202), and National Natural Science Foundation of China under Grant (51274016 and 51301128). Moreover, the authors also thank the financial support for this work from the Specialized Research Fund for the Doctoral Program of Higher Education of China under Grant (20110201130008), the National Science Foundation for Post-doctoral Scientists of China under Grants (2012M521767 and 2013T60875), Shaanxi provincial post-doctoral research project, and the Fundamental Research Funds of Xi'an Jiaotong University under Grant (XJJ2013038).

## References

1. A. Studnicki, J. Kilarski, M. Przybyl, J. Suchońand, and D. Bartocha, Wear Resistance of Chromium Cast Iron-Research and Application, *J. Achiev. Mater. Manuf. Eng.*, 2006, **16**, p 63–73
2. E. Zumelzu, I. Goyos, C. Cabezas, O. Opitz, and A. Parada, Wear and Corrosion Behaviour of High-Chromium (14-30% Cr) Cast Iron Alloys, *J. Mater. Process. Technol.*, 2002, **128**, p 250–255
3. R. Correa, A. Bedolla-Jacuinde, J. Zuno-Silva, E. Cardoso, and I. Mejia, Effect of Boron on the Sliding Wear of Directionally Solidified High-Chromium White Irons, *Wear*, 2009, **267**, p 495–504
4. H. Fu and J. Xing, *Manufacture Technology of Wear Resistant Casting*, Machinery Press, Beijing, 2009, p 20–30
5. O. Ozdemir, M. Usta, C. Bindal, and A.H. Ucisik, Hard iron boride ( $Fe_2B$ ) on 99.97 wt% pure iron, *Vacuum*, 2006, **80**, p 1391–1395
6. M. Ulutan, Y.M. Mustafa, N.C. Osman, and S. Buytoz, Tribological properties of borided AISI, 4140 steel with the powder packboriding method, *Tribol. Lett.*, 2010, **38**, p 231–239
7. Benxi Iron and Steel Co, *Boron Steel*, Metallurgical Industry Press, Beijing, 1977, p 2
8. D.W. Yi, J.D. Xing, and S.Q. Ma, Investigation on Microstructures and Two-Body Abrasive Wear Behavior of Fe-B Cast Alloy, *Tribol. Lett.*, 2011, **45**, p 427–435
9. Z.L. Liu, X. Chen, Y.X. Li, and K.H. Hu, Effect of Chromium on Microstructure and Properties of High Boron White Cast Iron, *Metall. Mater. Trans. A*, 2008, **39**, p 636–641
10. H.G. Fu and K.H. Hu, High boron Cast Iron Base Anti-wear Alloy and Its Heat Treatment Method, Chinese Patent, CN1624180-A, 2004
11. H.G. Fu and Z.Q. Jiang, A Study of Abrasion Resistant Cast Fe-B-C Alloy, *Acta Metall. Sin.*, 2006, **42**, p 545–548
12. H.G. Fu, A Study of High Boron Cast Steel Hammer, *Foundry*, 2006, **55**, p 292–295
13. H.G. Fu, Q. Xiao, J.C. Kuang, Z.Q. Jiang, and J.D. Xing, Effect of Rare Earth and Titanium Additions on the Microstructures and



- Properties of Low Carbon Fe-B Cast Steel, *Mater. Sci. Eng. A*, 2007, **466**, p 160–165
14. Chinese National Standard, GB/T 6394-2002, *Metal-Methods for Estimating the Average Grain Size*, Bureau of Quality Supervision, Inspection and Quarantine, Manual of Chinese National Standard, Beijing, 2002
  15. American Society for Testing and Materials, *ASTM E384-08, Standard Test Method for Microindentation Hardness of Materials*, American Society for Testing and Materials, West Conshohocken, PA, 2008
  16. D.W. Yi, J.D. Xing, H.G. Fu, S.Q. Ma, and Z.X. Liu, Effects of RE-Al Additions and Austenitising Time on Structural Variations of Medium Carbon Fe-B Cast Alloy, *Mater. Sci. Technol.*, 2010, **26**, p 849–857
  17. Z.S. Yu, *The Application of Rare Earth in Steel*, Metallurgical Industry Press, Beijing, 1987, p 231–237
  18. R. Chotěborský, B. Bryksí-Stunová, and M. Kolaříková, Effect of Rare Earth Element on Microstructure of Fe-B Cast Alloy, *22nd International Conference on Metallurgy and Materials (Metal 2013)*, May 15th-17th 2013, Brno, Czech Republic
  19. D.W. Yi, J.D. Xing, and S.Q. Ma, Three-Body Abrasive Wear Behavior of Low Carbon Fe-B Cast Alloy and Its Microstructures Under Different Casting Process, *Tribol. Lett.*, 2011, **42**, p 67–77
  20. J.J. Zhang, Y.M. Gao, J.D. Xing, S.Q. Ma, and D.W. Yi, Effects of Plastic Deformation and Heat Treatment on Microstructure and Properties of High Boron Cast Steel, *J. Mater. Eng. Perform.*, 2011, **20**, p 1658–1664
  21. D.W. Yi, J.D. Xing, H.G. Fu, S.Q. Ma, and Z.X. Liu, Effects of Rare Earth-Aluminium Additions on the Microstructure of a Semisolid Low Carbon Fe-B Cast Alloy, *Mater. Sci. Technol.*, 2011, **27**, p 1518–1526
  22. H. Qiu, H. Mori, M. Enoki, and T. Kishi, Fracture Mechanism and Toughness of the Welding Heat-Affected Zone in Structural Steel Under Static and Dynamic Loading, *Metall. Mater. Trans. A*, 2000, **31**, p 2785–2791
  23. T. Du, Physical-Chemistry Effect of Rare Earth Elements on Metallic Materials, *Acta Metall. Sin.*, 1997, **33**, p 69–77
  24. X.H. Zhi, J.D. Xing, H.G. Fu, and Y.M. Gao, Effect of Titanium on the As-Cast Microstructure of Hypereutectic High Chromium Cast Iron, *Tribol. Lett.*, 2008, **59**, p 1221–1226
  25. B.L. Bramfitt, The Effect of Carbide and Nitride Additions on the Heterogeneous Nucleation Behavior of Liquid Iron, *Metall. Trans.*, 1970, **1**, p 1987–1991
  26. Y.J. Tian, H.Q. Wu, J.H. Guo, and F.R. Li, Effect of RE Inclusions on Heterogeneous Nucleation of Primary Austenite in Fe-C Alloys, *J. Chinese Rare Earth Soc.*, 1988, **6(4)**, p 45–48